Detecting stress injury (fatigue fracture) in fibular cortical bone using quantitative ultrashort echo time magnetization transfer (UTE-MT): An ex vivo study

Saeed Jerban[1], **Yajun Ma**[1], **Amin Nazaran**[1], **Erik W. Dorthe**[2], **Esther Cory**[3], **Michael Carl**[4], **Darryl D'Lima**[2], **Robert L. Sah**[3,5], **Eric Y. Chang**[6,1], and **Jiang Du**[1]

[1]Department of Radiology, University of California, San Diego, CA, USA

[2]Shiley Center for Orthopedic Research and Education at Scripps Clinic, La Jolla, CA, USA

[3]Department of Bioengineering, University of California, San Diego, La Jolla, CA, USA

[4]GE Healthcare, San Diego, CA, USA

[5]Department of Orthopaedic Surgery, University of California, San Diego, La Jolla, CA, USA

[6]Radiology Service, VA San Diego Healthcare System, San Diego, CA, USA

Abstract

Bone stress injury (BSI) incidents have been increasing among athletes in recent years due to more intense sport activities. Cortical bone in the tibia and fibula are among the most common BSI sites. Nowadays, clinical MRI is the most recommended technique for BSI diagnosis at early stages. However, clinical MRI focuses on edema observations in surrounding soft tissues, rather than the injured components of the bone. Specifically, both normal and injured bone, are invisible in conventional clinical MRI. In contrast, ultrashort echo time (UTE) MRI is able to detect the rapidly decaying signal from the bone. This study aimed to employ UTE-MRI for fatigue fracture detection in fibula cortical bone, through an *ex vivo* investigation. Fourteen human fibulae samples (47±20 years old, 4 women) were subjected to cyclic loading on a 4-point bending setup. The loading was displacement controlled to induce -5000 ± 1500 μ-strain at 4 Hz. Loading was stopped when bone stiffness was reduced by 20%. Fibulae samples were imaged twice, using UTE-MRI and μCT, first pre-loading and second time, post-loading. After loading, macromolecular fraction (MMF), from UTE-MT modelling demonstrated a significant decrease $(12\pm20\%, P = 0.02)$ on average. Single-component T2* also decreased significantly by BSI $(12\pm11\%, P = 0.01)$ on average. MMF reduction is hypothesized to be a result of collagenous matrix rupture and water increase. However, faster T2* decay might be due to water shifts towards newly developed microcracks with higher susceptibility. Despite this good sensitivity level of the UTE-MRI technique, the μCT-based porosity at 9 μm voxel size was not affected by loading. UTE-MRI shows promise as a new quantitative technique to detect BSI.

Corresponding authors: Jiang Du, Department of Radiology, University of California, 9500 Gilman Dr, San Diego, CA 92093, USA, jiangdu@ucsd.edu, Phone: 619-471-0519, Fax : +1 888 960 5922; Saeed Jerban, Department of Radiology, University of California, 9500 Gilman Dr, San Diego, CA 92093, USA, sjerban@ucsd.edu, Phone : +1 858 642 1211, Fax : +1 888 960 5922.

[6]·Conflict of interest statement
The authors have no conflict of interests to mention.

Keywords

Bone stress injury; fatigue fracture; MRI; cortical bone; ultrashort TE; magnetization transfer

1. Introduction

Bone stress injury (BSI) is commonly seen among highly active individuals [1–5]. In elite athletes, the incidence rate of BSI has been increasing due to longer and more intense sport activities [6]. Fatigue- , insufficiency-, pseudo-, overuse-, exhaustion-, and marching-fractures are other terms used in the literature for BSI [7,8]. Major factors leading to BSI include training cycles, bone health, gender, diet, biomechanics and footwear [5,8–12].

BSI is initiating by repeated sub-maximal mechanical loads and results in load-related pain [1–4,13]. BSI generally occurs in a few weeks after commencement of intense training [1]. The pain develops gradually in BSI, first presenting only during loading and later occurring also at rest [1]. The incidence rate of BSI correlates highly with the cumulative running in athletes [14].

Bone remodeling, driven by mechanical loading, is continuously orchestrating the bone microstructure. From a biomechanical point of view, the interplay between (1) the high number of load cycles [15], (2) the muscle exhaustion [5,16], (3) the accelerated bone resorption process [1] and (4) the local temporal hypoxia [4] ends in BSI. Specifically, all mentioned phenomena may end in ruptures in the collagenous matrix and occurrence of a set of cracks from hundreds of nanometers to tens of micrometers in size [17,18].

The common locations of BSI are highly related with the type of the exercise [1–4,16]. The long bones of the lower limbs (tibia and fibula), are common sites of BSI occurrence in basketball players and runners [2,3,5,19–21]. The tibia itself accounts for 40–60 % of cases of BSI in runners [4,6,16]. BSI in the fibula presents similar characteristics, yet with a lower rate of incidence (6–24% of lower limb BSIs) compared with tibial BSI [2]. In theory, all long bones are susceptible to BSI due to their similar underlying anatomical morphology and biomechanics.

Early stage diagnosis of BSI is crucial for optimizing treatment and return to play time. In competitive athletes, the return to play time ranges from weeks to months [5]. A premature return to activity may in fact increase the risk of recurrent BSIs [11]. BSIs should be distinguished from bone stress reactions that are normally accompanied with some edema, yet display a different set of characteristics. Physical examination is the first step towards the diagnosis of BSI; however, imaging modalities are crucial to confirm the BSI status. Conventional radiography, CT, musculoskeletal ultrasonography, scintigraphy, and MRI, are common techniques to diagnose the BSI [1,6,13,16,22–24].

Since the late 1990s, clinical MRI has become the most common modality for early stage diagnosis of BSI [1,6,13,16,22–26]. Clinical T1 and T2 weighted images are recognized as the most practical techniques for detecting BSI during the first 3 weeks of onset [1,13] through edema detection in periosteum and bone marrow [1,10,13,27,28]. Nevertheless, clinical MRI

lacks any quantitative assessment of the injured components of the bone, because, normal and injured bones are "invisible" on clinical MRI. Specifically, cortical bone possesses a very short T2*, such that clinical MRI renders the cortical bone with very low signal, similar to the background [29,30]. Consequently, an MRI-based quantitative assessment of the injured bone is of great interest to orthopaedic researchers and surgeons, which can improve the early stage diagnosis and quantification of BSI as well as longitudinal follow-up in athletes recovering from BSI.

Ultrashort echo time MRI (UTE-MRI) sequences can be used to image and quantitatively assess the cortical bone [29–39] as well as other musculoskeletal tissues such as tendon and cartilage [29,40]. UTE-MRI can detect signal from both bound water and pore water in the cortical bone [29,30,33,36,37]. T2* of bound water is approximately one tenth of T2* of pore-water in the cortical bone [29,30,33,36] that enables separating bound and pore water, using bi-component modeling of UTE-T2* signal decay. Bound water can also be selectively imaged via an Inversion Recovery UTE (IR-UTE) sequence by inverting and then nulling the signal from the pore-water [31,38,41–43]. Figure 1 shows an exemplary axial imaging of the leg of a healthy volunteer from a clinical gradient echo sequence compared with UTE and IR-UTE sequences. Despite the signal void of tibial and fibular cortex on clinical MRI (Figure 1a), UTE-MRI and IR-UTE-MRI demonstrate a high signal and contrast in cortical bone (Figure 1a,b). Moreover, magnetization transfer (MT) imaging combined with UTE technique can be used for systematic evaluation of the MT effects in bone, including macromolecular fraction (MMF) and macromolecular T2 ($T2_{MM}$) obtained from two-pool MT modeling[34,44]. Although the UTE-MRI techniques have been used extensively to assess cortical bone [30,35,41,42,45–50], the changes in UTE-MRI properties following BSI are yet to be investigated.

The main objective of this study was to determine whether UTE-MRI biomarkers are sensitive to changes induced by BSI, such as cortical bone microcracks and collagen fibril ruptures. An experimental protocol was planned to create limited fatigue fractures, resembling early stage BSI, in the midshaft of human fibulae. The investigated biomarkers here include UTE-T2*, T1 and two-pool MT modeling analyses.

2. Materials and methods

2.1. Sample preparation

Cortical bone samples were harvested from the midshaft fibulae of fourteen fresh-frozen donors (47±20 years old, 4 women) obtained from a nonprofit whole-body donation company (United Tissue Network, Phoenix, AZ). The donor's lower legs underwent one freezing and thawing cycle. Fibulae midshafts were cut into 4 cm lengths using a bandsaw (Shopmaster, Delta Machinery, Tennessee, USA). Bone marrow and trabeculae were gently cleaned with a scalpel from the cortical bone. All samples were initially scanned using UTE-MRI as described below in sections 2.2. The samples were scanned again, after they underwent a cyclic loading experiment to induce fatigue fractures representing 20% reduction of bone stiffness (section 2.4).

2.2. UTE-MR imaging

All fibulae samples were immersed in phosphate-buffered saline (PBS) for 2 hours at room temperature before the MRI scans. Each sample was placed in a 30-mL syringe, filled with perfluoropolyether (Fomblin, Ausimont, Thorofare, NJ) to minimize dehydration and susceptibility artifact. The specimens were imaged in the sagittal plane on a 3T clinical MRI scanner (Signa HDx, GE Healthcare Technologies, Milwaukee, WI) using a home-made 1-inch diameter solenoid transmit/receive (T/R) coil. A quantitative imaging protocol was performed, consisting of I) a dual-echo 3D-UTE-Cones sequence (TR = 30 ms, TEs = 0.032, 0.2, 0.4, 0.6, 0.8, 2.2, 4.4, 6.6, 8.8, 11, 13, and 15 ms, flip angle (FA) = 10˚, rectangular RF pulse with a duration of 28 μs) for T2* measurements (bound and pore water), II) a variable TR 3D-UTE-Cones sequence (TE = 0.032 ms, TRs = 5.9, 10, 20, 40, 60, and 100 ms, FA = 20˚, rectangular RF pulse with a duration of 28 μs) for T1 measurement, and III) a 3D-UTE-MT-Cones sequence (MT saturation pulse power = 500°, 750°, and 1000°, frequency offset = 2, 5, 10, 20, and 50 kHz, FA = 10˚, rectangular RF pulse with a duration of 28 μs) for two-pool MT modelling. Other imaging parameters include field of view (FOV) = 4 cm, matrix = 192×192, slice thickness = 3 mm, and receive bandwidth = 62.5 kHz. It should be noted that the nominal TEs are measured from the end of the RF pulse to the start of data sampling. All MRI scans were repeated after the loading experiment. The details of the dual-echo, inversion recovery, and variable TR 3D-UTE-Cones sequences have been discussed in previous studies [29–31,51]. The two-pool UTE-MT modeling was previously described in detail by Ma et al. [34,44]. Specifically, the contrast in two-pool MT model is based on the interactions between macromolecular and water protons.

2.3. Microcomputed tomography (μCT)

Four fibula samples from the total fourteen, were randomly selected and scanned using a Skyscan 1076 (Kontich, Belgium) μCT scanner at 8.78 μm isotropic voxel size, before and after cyclic loading. This was to examine the μCT capability in detecting the microfracture, even though, literature has shown that μCT is incapable of detecting microfractures in such a resolution [18,52]. Other scanning parameters were as follows: a 0.05 mm aluminum plus 0.038 mm copper filter, 100 kV, 100 mA, 0.6˚ rotation step, 3 frame-averaging, 3.5 hours total scan time per sample. Samples were kept humid in a sealed container to avoid dehydration during the μCT scans.

2.4. Fatigue fracture induction (cyclic loading)

The bone samples were subjected to a cyclic loading session using a 4-point bending set up (ASTM D790) to induce a limited fatigue fracture (Figure 2). The jig setup comprised of four tungsten pins (3-mm diameter) held in two aluminum seats. The upper aluminum seat connected to the actuator and the lower aluminum seat connected to the load cell. The 4-point bending jig was mounted onto a mechanical testing machine (model 8511.20, Instron, Norwood, MA, USA) including a 100 Newton load cell (Instron 2519–103) with an actuator displacement accuracy of <0.002 mm. The loading was displacement controlled and involved 1) finding contact, 2) applying approximately −5000 μstrain, by manually adjusting the actuator, 3) applying a sinusoidal displacement to generate −5000 ± 1500 μstrain at 4 Hz. A preconditioning cyclic loading was applied for 1000 cycles before the main loading

experiment. The main cyclic loading was stopped by the operator once the monitored bone stiffness (real time measured from strain stress curves) decreased to below 80% of the initial bone stiffness (elastic modulus). On average, the cyclic loading was stopped after approximately 150 minutes. Schematics of the reduction in measured load due to microcracks induced in bone is depicted in Figure 2a.

2.5. Data analysis

MRI data analyses were performed for a selected section (3 mm thick) between the two loading pins (Section A-A in Figure 2a) in each one of the fibulae samples. For each MRI dataset, two regions of interest (ROIs) were selected (Figure 3a) such that A and B covered the compression (upper) and tension (lower) sides of fibula samples in 4-point bending test. Selected ROIs were large enough to avoid being disturbed by pixel wise variations in bone specimens (i.e., 120±20 pixels, approximately ¼ the total cross section). Specifically, selected ROIs within post-loading datasets were used to generate ROIs within pre-loading datasets, through an image registration process.

The mean values of single-component T2*, bi-component-T2* results, T1, and MT modelling results within selected ROIs, were compared between pre- and post-loading datasets. All data analyses were performed using MATLAB (version 2016, Mathworks, Natick, MA, USA).

2.5.1. UTE-T2* measurements—Single-component ($S(TE) \propto \exp(-TE/T2^*) + constant$) and bi-component ($S(TE) \propto F_S \times \exp(-TE/T2_S^*) + F_L \times \exp(-TE/T2_L^*) + constant$) fitting models were utilized for T2* decay analyses acquired from dual-echo 3D-UTE-Cones sequence. In contrast to single-component analysis, bi-component analysis of T2* provides information on the short T2* (bound water) and long T2* (pore water) pools, separately

2.5.2. UTE-MT measurements—The acquired data with the set of MT saturation pulse powers (500°, 750°, and 1000°) and frequency offsets (2, 5, 10, 20, and 50 kHz) were fitted by a modified rectangular pulse approximation (mRP) approach which was previously described [30] . In this model, the loss rate of longitudinal magnetization of the macromolecular pool due to the RF saturation of the MT pulse is fitted by a Gaussian line shape function. Consequently, the parameters including macromolecular fraction and macromolecular T2 can be estimated as described by Ma et al. [44]. As a prerequisite for UTE-MT modeling, T1 was analyzed from 3D-UTE-Cones images acquired with variable TRs using single-component fitting ($S(TR) \propto (1 - \exp\left(-\frac{TR}{T1}\right)) + constant$). Details of these relaxometry analyses have been provided in previous studies [29,30,55]. The UTE-MT analysis was performed offline on the acquired DICOM images using an in-house code written in MATLAB (version 2016, Mathworks, Natick, MA, USA).

2.5.3. Bone porosity measurements—The μCT data were processed to calculate the porosity pixel map for an axial 3-mm slice (340 sections, each 8.87 μm thick) of the selected 4 bone samples. A gray level threshold was used for image segmentation to distinguish between cortical bone and pores. This threshold was selected for each set of data (340 μCT

sections) using the peaks of gray level histograms and visual inspection of the raw images. The porosity pixel maps were generated by superimposing all the 340 binary images. Affine image registration was used to propagate the ROIs used for MRI analysis to the μCT data.

2.6. Statistical Analysis

All statistical analyses were performed using a statistical programming language (R, version 3.2.5, R Development Core Team, Vienna, Austria). The differences in single-component T2*, bi-component-T2* results, T1, and MT modelling results were compared between pre- and post-loading datasets using a paired Wilcoxon Rank-Sum test. Shapiro-Wilk test application showed earlier that the data was not normally distributed in this study (P>0.05). The results were specifically compared for average values, compression side, and tension side of the fibula samples. P-values below 0.05 were considered significant.

3. Results

Figure 3 illustrates the representative MRI-based analyses for a selected axial section (Sec A-A in Figure 2a) at the middle of sample I. As shown in Figure 3a, the analyses were performed in two ROIs at compression and tension sides (ROI-A and ROI-B). Figure 3b shows the bi-component T2* decay analyses in ROI-A. Bi-component analysis provides the T2* values and corresponding fractions for bound water and pore-water, respectively. Figure 3c illustrates the T1 recovery using a single-component fitting for variable TRs (5.7 to 100 ms). MT modeling analysis in ROI-A is shown in Figure 3d for three MT saturation pulse powers (500°, 750° and 1000°) and five off-resonance frequencies (2, 5, 10, 20, and 50 kHz).

The summarized results of the single- and bi-component T2*, T1, MT modeling, and MTR T2* measurements for all fibulas are presented in Table 1 for pre- and post-loading datasets. The average variations of UTE properties by the loading experiments as well as the corresponding statistical significances (Paired Wilcoxon Rank-Sum Test) are presented in Table 2. The variations were calculated for i) average value per samples, ii) compression side (ROI-A), and iii) tension side (ROI-B).

For average results, MMF decreased significantly by 12±20% (P = 0.02). The MMF reduction was less in compression side ROIs (9±23%, P = 0.15) compared with tension side ROIs (14±15%, P = 0.08). For average results, single-component T2* values decreased significantly by the loading experiment, by 12±11% (P = 0.01). Single-component T2* reduction was higher for compression side ROIs (15±10%, P = 0.03) compared with tension side ROIs (10±11%, P = 0.28).

Other UTE-MRI parameters presented noticeable yet not significant variations on average after cyclic loading (Table 2). MTR values reduced on average for all selected MT pulse powers and frequency offsets. The MTR variations were higher in tension side ROIs compared with the compression side ROIs. From bi-component T2* analyses, short component T2* (T2*-S) decreased after loading on average while its fraction (Frac-S) increased. Long component T2* (T2*-L) also showed a decrease by loading.

Figure 4 shows MMF and single component T2* pixel maps of a representative sample (i.e., sample I) for pre- and post-loading datasets. The anticipated reductions in MMF and T2* values from Table 1 and 2, are obvious in depicted maps.

Table 3 presents the μCT-based porosities of the four selected fibulae samples for pre- and post-loading datasets. The average porosity varied from 1.8±0.6% to 1.6±0.7 (P = 0.89). The porosity varied from 1.2±0.6% to 1.6±0.9 (P = 0.49) and from 2.4±1.1% to 1.6±1.2 (P = 0.17), for compression and tension sides ROIs. All μCT-based porosity variations were found to be nonsignificant.

4. Discussion

UTE-MRI based biomarkers were studied, for the first time, to detect partial fatigue fractures in cortical bone, as an early stage of the BSI. UTE-MRI had been used to assess cortical bone microstructural and mechanical properties by different research groups [29,30,35,41,42,45,47–50]. However, UTE-MRI has not been used for bone fatigue fracture detection.

Conventional radiography, CT, musculoskeletal ultrasonography, scintigraphy, and MRI are clinical techniques that have been used to detect BSI. Conventional radiographs, as the first routine imaging modality, may detect the BSI, 2–12 weeks after the onset. The first radiographic sign is a low-density area in the cortical bone. The sensitivity of radiography is 15–35% in the early stages of BSI [1,6,13,16,22–24]. CT may be less sensitive than conventional radiography for the diagnosis of BSI. However, certain fracture lines, can be seen more clearly with CT [13,16,22–24]. Scintigraphy (radionuclide bone scan) had been considered to be the best diagnostic method for BSI, with reported sensitivity close to 100%, but with high false positive diagnosis [1,6,13,16,23,24,56]. Scintigraphy can show an increase in bone uptake as early as 6–72 hours after the onset of pain [1,6,13,16,23,24]. The high radiation dose in scintigraphy is another important concern in addition to the high false diagnosis rate [24]. Musculoskeletal ultrasonography for BSI diagnosis remains in an early investigation stage [13,24].

Clinical MRI (e.g., T1-weighted and fluid-sensitive images) has been recommended for detecting early stage BSI, through observations of edema in and around the periosteum and bone marrow [1,13]. Fredericson et al. [57] developed a grading approach for BSI (4 grades), based on the edema observations in MRI. Later, Kijowski et al. [27] improved and simplified the Fredericson grades, based on the return to play time. They suggested combining three of the grades that have similar degrees of periosteum and bone marrow edema and similar time to return (2 grades instead of 4 Grades). Semi-quantitative approaches (grading), have been the most systematic methods in MRI-based diagnosis of BSI [1,10,13,27,28], however, these grades fail to quantify the extent of injury to the bone.

All hypothesized mechanisms for BSI may end in collagenous matrix rupture and bone microcracks at the early stages. Such microcracks may occur at different scales: microstructural and ultrastructural levels [17,18]. At the microstructural level, cracks can be 20–100 μm long in the transverse plane of cortical bone, and reach 500–1000 μm in the

longitudinal plane (88 ± 21 and 488 ± 151 μm width and length, respectively [17]). However, the thickness of microcracks might only be a few micrometers. At the ultrastructural level, numerous nanocracks might be grouped and result in short arrays (< 10 μm long), visible on histology images [18]. Fatigue fractures accompany with reduction in the bone stiffness and initiate with cracks at the ultrastructural level that later evolve into cracks at the microstructural level [18,52].

Our cyclic loading experiment led to a partial fatigue fracture in cortical bone that resembled the early stages of BSI. The fatigue fracture was implied by the 20% reduction in monitored bone stiffness. As reported in the literature, the bone stiffness reduction via cyclic loading is always accompanied with the presence of the microcracks [52,58–61]. A few UTE-MRI quantitative properties of post-loading bone samples demonstrated significant changes compared with the pre-loading samples.

MMF, from two-pool MT modelling, presented a significant reduction on average in bone specimens after loading ($12 \pm 20\%$, P = 0.02, Table 2). The MMF reduction was higher for tension side ROIs compared with compression side ROIs ($14 \pm 15\%$ versus $9 \pm 23\%$, Table 2). Significant MMF reduction probably indicates collagenous matrix rupture or collagen softening. Probable higher water loss in compression side ROIs is expected to downgrade the MMF variations. MTR reductions by the induced fatigue fracture also imply collagenous matrix rupture, even though the variations were not significant (Table 2). Evidently, more sophisticated analyses of MT signal, such as the presented UTE-MT modeling, demonstrated stronger potential to sense the complex nature of the BSI, which is not limited to water redistribution or collagenous matrix rupture.

Single-component T2* significantly decreased in the bone samples ($12 \pm 11\%$, P = 0.01, Table 2). T2*-S From bi-component decreased after loading on average while its fraction (Frac-S) increased. Long component T2* (T2*-L) also showed a decrease by loading. Such T2* reductions most likely demonstrate water shifts towards the generated micro- and nanocracks with higher susceptibility, which in turn resulted in faster T2* decay.

The μCT-based porosity variation in four selected specimens was not statistically significant and consistent (Table 3). In fact, μCT at 8.78 μm voxel size, was limited to detect, not only the micro- and nanocracks, but also many of original pores in the cortical bone. Specifically, the cracks induced by the cyclic loading, resulting in 20% reduction of bone stiffness, were expected to be in ultrastructure level, which may not be detectable by μCT. In the same way, Burr et al. [52], did not observe significant microdamage at the light microscopy level (submicron pixel size) until there was a 15% decrease in canine bone stiffness [18,52]. On the other hand, Landrigan et al. [60] and Travis et al. [61] were able to detect microcracks induced by 5–10% reduction of bone stiffness, using a μCT dataset at 10 μm voxel size, but only when barium sulfate (BaSO4) contrast agent was administered.

Our results indicate that quantitative UTE-MT-MRI has great potential to serve as a new class of diagnostic techniques for BSI at the early stages (i.e., fatigue fracture). Quantitative UTE-MT-MRI technique complemented with clinical MRI (detecting edema in surrounding soft tissue) could be an accurate and comprehensive diagnostic method and deserves further

study. UTE-MT modeling results, particularly MMF, was found to vary significantly in damaged locations of cortical bone.

In vivo BSI is expected to be slightly different from the ex vivo BSI presented in this study. The response from the peripheral soft tissue environment as well as biologic and immune system would be enhancing cellular activities, uptake, and intraosseous hydrostatic pressures [1]. Such enhancements can explain the developing edemas around injured bone in patients [1,13]. Moreover, cellular resorption process triggered by the excessive loading in bone, is expected to initiate BSI [1,4,56]. All aforementioned phenomena are expected to result in higher water concentration around injured in vivo bone. Thus a larger MMF reduction is anticipated for in vivo BSI compared with observed reductions in this study for ex vivo BSI.

A constant offset was introduced in the fitting models which may lead to an overestimate of the relaxation times due to the Rician distributed noise contribution. However, the noise distribution in 3D UTE images is more complicated than conventional Cartesian images. Streak artifacts associated with spiral sampling may affect the noise distribution. The introduction of a constant term seems helpful to account for the contribution from artifacts associated with spiral sampling and imperfect regridding reconstruction. Considering a constant contribution of the noise to the MRI signal might slightly overestimate the relaxation times in this study. Nonetheless, the overestimations are consistent and can be neglected when the variation of the relaxation times are the focus of the study.

This study has several limitations as follows. First, the fibula samples possessed a variety of shapes that may not be perfectly mounted on the four-point bending jigs. Therefore, the load might not be distributed evenly between pins (Figure 2a) for all samples, which eventually challenged the accurate localizing of anticipated fractures. Preparing rectangular slabs of cortical bone from tibia for future studies is recommended. Second, the level of the induced microdamage in bone was not sufficient to be detected in μCT at 9-micron voxel size. Further studies are worthy to investigate higher levels of bone stiffness reduction with higher μCT resolution, probably with contrast agents, in addition to histological studies. Three-dimensional histomorphometric measures of microcracks (number and volume) should be correlated with the UTE-MRI biomarkers as well as the induced BSI severity level to find out which combination of parameters can provide the highest sensitivity and specificity for BSI diagnosis. Indeed, the MRI properties are not independent from each other, and an optimum combination of them might be practical to assess BSI. Third, this study was performed on ex vivo cortical bone and lacked the peripheral soft tissue environment as well as biologic and immune system reactions after fatigue fracture incidence. Thus, herein presented results and hypotheses need to be validated in a well-designed in vivo animal model or human study.

5. Conclusion

UTE-MRI was used, for the first time, to detect fatigue fracture in cortical bone in an ex vivo study. UTE-MRI based biomarkers in fibulae samples changed significantly after cyclic loading, which induced fatigue fracture in bone samples. MMF, from MT modeling outputs, significantly decreased by ex vivo BSI. MMF reduction most likely resulted from

collagenous matrix rupture. Single-component T2* values of bone samples demonstrated a significant decrease, that probably implies water shifts towards the generated micro- and nanocracks with higher susceptibility, which in turn resulted in faster T2* decay. As expected, μCT performed on the representative specimens was not sensitive to the fatigue fracture at the examined resolution. UTE-MT modeling was found capable of detecting fatigue fracture in cortical bone. UTE-MT may be recommended as a complementary technique to improve the accuracy and precision of BSI diagnosis at early stages.

Acknowledgements

Abbreviations:

BSI	bone stress injury
3D	three-dimensional
3D UTE	three-dimensional ultrashort echo time imaging
3D IR-UTE	three-dimensional adiabatic inversion recovery ultrashort echo time
FOV	field of view
IR	inversion recovery
MR	magnetic resonance
MRI	magnetic resonance imaging
MT	magnetization transfer
MTR	magnetization transfer ratio
PBS	phosphate buffered saline
RF	radio frequency
ROI	region of interest
TE	echo time
μCT	micro computed tomography
CT	computed tomography
MMF	macromolecules fraction

8. References

1. Lassus J, Tulikoura I, Konttinen YT, Salo J, Santavirta S. Bone stress injuries of the lower extremity: a review. Acta Orthop Scand. 2002;73(3):359–368. doi:10.1080/000164702320155392. [PubMed: 12143987]

2. Welck MJ, Hayes T, Pastides P, Khan W, Rudge B. Stress fractures of the foot and ankle. Injury. 2015. doi:10.1590/1806-9282.60.06.006.

3. Magnotti T How Serious Are Stress Fractures For NBA Players? http://hoopshabit.com/2014/06/23/serious-stress-fractures-nba-players/. Published 2014.

4. Romani WA, Gieck JH, Perrin DH, Saliba EN, Kahler DM, Anonymous. Mechanisms and management of stress fractures in physically active persons. J Athl Train. 2002;37(3):306–314. [PubMed: 16558676]

5. Behrens SB, Deren ME, Matson A, Fadale PD, Fadale KO. Stress fractures of the pelvis and legs in athletes: a review. Sports Health. 2013;5(2):165–174. doi:10.1177/1941738112467423. [PubMed: 24427386]

6. Mayer SW, Joyner PW, Almekinders LC, Parekh SG. Stress Fractures of the Foot and Ankle in Athletes. Sports Health. 2013;6(6):481–491. doi:10.1177/1941738113486588.

7. Kiuru MJ, Pihlajamäki HK, Ahovuo JA. Bone Stress Injuries. Acta radiol. 2004;45(3):000–000. doi:10.1080/02841850410004724.

8. Reinking MF, Austin TM, Bennett J, Hayes AM, Mitchell WA. Lower extremity overuse bone injury risk factors in collegiate athletes: a pilot study. Int J Sports Phys Ther. 2015;10(2):155–167. http://www.pubmedcentral.nih.gov/articlerender.fcgi?artid=4387723&tool=pmcentrez&rendertype=abstract. [PubMed: 25883864]

9. Barrack michelle T, Gibbs JC, De Souza MJ, et al. Higher Incidence of Bone Stress Injuries With Increasing Female Athlete Triad– Related Risk Factors. Am J Sports Med. 2014;42(4):949–958. doi:10.1177/0363546513520295. [PubMed: 24567250]

10. Nattiv A, Kennedy G, Barrack MT, et al. Correlation of MRI grading of bone stress injuries with clinical risk factors and return to play: a 5-year prospective study in collegiate track and field athletes. Am J Sports Med. 2013;41(8):1930–1941. doi:10.1177/0363546513490645. [PubMed: 23825184]

11. Lee K, Park Y, Jegal H, Kim K, Young K, Kim J. Factors Associated With Recurrent Fifth Metatarsal Stress Fracture. Foot Ankle Int. 2013;34(12):1645–1653. doi:10.1177/1071100713507903. [PubMed: 24216284]

12. Bui-Mansfield LT, Thomas WR. Magnetic resonance imaging of stress injury of the cuneiform bones in patients with plantar fasciitis. J Comput Assist Tomogr. 2009;33(4):593–596. doi:10.1097/RCT.0b013e31818af248. [PubMed: 19638857]

13. McInnis KC, Ramey LN. High-Risk Stress Fractures: Diagnosis and Management. Phys Med Rehabil. 2016;8(3, Supplement):S113–S124. doi:10.1016/j.pmrj.2015.09.019.

14. Armstrong DW, Rue JPH, Wilckens JH, Frassica FJ. Stress fracture injury in young military men and women. Bone. 2004;35(3):806–816. doi:10.1016/j.bone.2004.05.014. [PubMed: 15336620]

15. Anderson MW, Greenspan A. Stress fractures. Radiol Clin North Am. 1996;1999:1–12.

16. Asano L, Duarte J., APS S. Stress fractures in the foot and ankle of athletes. rev assoc med bras. 2014;60(6):512–517. pm:19680111. [PubMed: 25650848]

17. Mohsin S, O'brien FJ, Lee TC. Microcracks in compact bone: A three-dimensional view. J Anat. 2006;209(1):119–124. doi:10.1111/j.1469-7580.2006.00554.x. [PubMed: 16822275]

18. Donahue SW, Galley S a. Microdamage in bone: implications for fracture, repair, remodeling, and adaptation. Crit Rev Biomed Eng. 2006;34(3):215–271. doi:10.1615/CritRevBiomedEng.v34.i3.20. [PubMed: 16930125]

19. Niva MH, Sormaala MJ, Kiuru MJ. Bone Stress Injuries of the Ankle and Foot An 86-Month Magnetic Resonance Imaging – based Study of Physically Active Young Adults. Am J Sports Med. 2007;35(4):643–649. doi:10.1177/0363546506295701. [PubMed: 17099238]

20. Hong SH, Chu IT. Stress fracture of the proximal fibula in military recruits. Clin Orthop Surg. 2009;1(3):161–164. doi:10.4055/cios.2009.1.3.161. [PubMed: 19885052]

21. Wilson ES, Katz FN. Stress Fractures. Radiology. 1969;92(3):481–486. [PubMed: 5774957]

22. Astur DC, Zanatta F, Arliani GG, Moraes ER, Pochini A de C, Ejnisman B. Stress fractures: definition, diagnosis and treatment. Rev Bras Ortop (English Ed. 2016;51(1):3–10. doi:10.1016/j.rboe.2015.12.008.

23. Patel DS, Roth M, Kapil N. Stress fractures: diagnosis, treatment, and prevention. Am Fam Physician. 2011;83(1):39–46. [PubMed: 21888126]

24. Pegrum J, Crisp T, Padhiar N. Diagnosis and management of bone stress injuries of the lower limb in athletes. BMJ. 2012;344(424 3):e2511–e2511. doi:10.1136/bmj.e2511. [PubMed: 22532009]

25. Gmachowska A, Zabicka M, Pacho R. MRI findings of tibial stress injuries. Eur Soc Radiol. 2014:1–26.

26. Gaeta M, Minutoli F, Scribano E, et al. CT and MR imaging findings in athletes with early tibial stress injuries: comparison with bone scintigraphy findings and emphasis on cortical abnormalities. Radiology. 2005;235(2):553–561. doi:10.1148/radiol.2352040406. [PubMed: 15858094]

27. Kijowski R, Choi J, Shinki K, Del Rio AM, De Smet A. Validation of MRI classification system for tibial stress injuries. Am J Roentgenol. 2012;198(4):878–884. doi:10.2214/AJR.11.6826. [PubMed: 22451555]

28. Ruohola J-PS, Kiuru MJ, Pihlajamäki HK. Fatigue bone injuries causing anterior lower leg pain. Clin Orthop Relat Res. 2006;444(444):216–223. doi:10.1097/01.blo.0000194668.70225.24. [PubMed: 16523142]

29. Chang EY, Du J, Chung CB. UTE imaging in the musculoskeletal system. J Magn Reson Imaging. 2015;41(4):870–883. doi:10.1002/jmri.24713. [PubMed: 25045018]

30. Du J, Bydder GM. Qualitative and quantitative ultrashort-TE MRI of cortical bone. NMR Biomed. 2013;26(5):489–506. doi:10.1002/nbm.2906. [PubMed: 23280581]

31. Du J, Hermida JC, Diaz E, et al. Assessment of cortical bone with clinical and ultrashort echo time sequences. Magn Reson Med. 2013;70(3):697–704. doi:10.1002/mrm.24497. [PubMed: 23001864]

32. Diaz E, Chung CB, Bae WC, et al. Ultrashort echo time spectroscopic imaging (UTESI): an efficient method for quantifying bound and free water. NMR Biomed. 2012;25(1):161–168. doi:10.1002/nbm.1728. [PubMed: 21766381]

33. Du J, Carl M, Bydder M, Takahashi A, Chung CB, Bydder GM. Qualitative and quantitative ultrashort echo time (UTE) imaging of cortical bone. J Magn Reson. 2010;207(2):304–311. doi:10.1016/j.jmr.2010.09.013. [PubMed: 20980179]

34. Ma Y-J, Shao H, Du J, Chang EY. Ultrashort echo time magnetization transfer (UTE-MT) imaging and modeling: magic angle independent biomarkers of tissue properties. NMR Biomed. 2016;29(11):1546–1552. doi:10.1002/nbm.3609. [PubMed: 27599046]

35. Rajapakse CS, Bashoor-Zadeh M, Li C, Sun W, Wright AC, Wehrli FW. Volumetric Cortical Bone Porosity Assessment with MR Imaging: Validation and Clinical Feasibility. Radiology. 2015;276(2):526–535. doi:10.1148/radiol.15141850. [PubMed: 26203710]

36. Seifert AC, Wehrli FW. Solid-State Quantitative 1H and 31P MRI of Cortical Bone in Humans. Curr Osteoporos Rep. 2016:1–10. doi:10.1007/s11914-016-0307-2. [PubMed: 26861807]

37. Granke M, Does MD, Nyman JS. The Role of Water Compartments in the Material Properties of Cortical Bone. Calcif Tissue Int. 2015;97(3):292–307. doi:10.1007/s00223-015-9977-5. [PubMed: 25783011]

38. Manhard MK, Horch RA, Harkins KD, Gochberg DF, Nyman JS, Does MD. Validation of quantitative bound- and pore-water imaging in cortical bone. Magn Reson Med. 2014;71(6):2166–2171. doi:10.1002/mrm.24870. [PubMed: 23878027]

39. Nyman JS, Ni Q, Nicolella DP, Wang X. Measurements of mobile and bound water by nuclear magnetic resonance correlate with mechanical properties of bone. Bone. 2008;42(1):193–199. doi:10.1016/j.bone.2007.09.049. [PubMed: 17964874]

40. Jerban S, Nazaran A, Cheng X, et al. Ultrashort echo time T2* values decrease in tendons with application of static tensile loads. J Biomech. 2017;61:160–167. doi:10.1016/j.jbiomech.2017.07.018. [PubMed: 28780188]

41. Li C, Seifert AC, Rad HS, et al. Cortical Bone Water Concentration: Dependence of MR Imaging Measures on Age and Pore Volume Fraction. Radiology. 2014;272(3):796–806. doi:10.1148/radiol.14132585. [PubMed: 24814179]

42. Horch RA, Gochberg DF, Nyman JS, Does MD. Clinically compatible MRI strategies for discriminating bound and pore water in cortical bone. Magn Reson Med. 2012;68(6):1774–1784. doi:10.1002/mrm.24186. [PubMed: 22294340]

43. Larson PEZ, Conolly SM, Pauly JM, Nishimura DG. Using adiabatic inversion pulses for long-T2 suppression in ultrashort echo time (UTE) imaging. Magn Reson Med. 2007;58(5):952–961. doi: 10.1002/mrm.21341. [PubMed: 17969119]

44. Ma Y-J, Chang EY, Carl M, Du J. Quantitative magnetization transfer ultrashort echo time imaging using a time-efficient 3D multispoke Cones sequence. Magn Reson Med. 2017;00:1–9. doi: 10.1002/mrm.26716.

45. Chang EY, Bae WC, Shao H, et al. Ultrashort echo time magnetization transfer (UTE-MT) imaging of cortical bone. NMR Biomed. 2015;28(4):873–880. doi:10.1002/nbm.3316. [PubMed: 25981914]

46. Li S, Chang EY, Bae WC, et al. Ultrashort echo time bi-component analysis of cortical bone - A field dependence study. Magn Reson Med. 2014;71(3):1075–1081. doi:10.1002/mrm.24769. [PubMed: 23630048]

47. Bae WC, Chen PC, Chung CB, Masuda K, D'Lima D, Du J. Quantitative ultrashort echo time (UTE) MRI of human cortical bone: Correlation with porosity and biomechanical properties. J Bone Miner Res. 2012;27(4):848–857. doi:10.1002/jbmr.1535. [PubMed: 22190232]

48. Rad HS, Lam SCB, Magland JF, et al. Quantifying cortical bone water in vivo by three-dimensional ultra-short echo-time MRI. NMR Biomed. 2011;24(7):855–864. doi:10.1002/nbm.1631. [PubMed: 21274960]

49. Horch RA, Gochberg DF, Nyman JS, Does MD. Non-invasive predictors of human cortical bone mechanical properties: T2-Discriminated 1H NMR compared with high resolution X-ray. PLoS One. 2011;6(1):1–5. doi:10.1371/journal.pone.0016359.

50. Chen J, Grogan SP, Shao H, et al. Evaluation of bound and pore water in cortical bone using ultrashort-TE MRI. NMR Biomed. 2015;28(12):1754–1762. doi:10.1002/nbm.3436. [PubMed: 26527298]

51. Nazaran A, Carl M, Ma Y-J, et al. Three-dimensional adiabatic inversion recovery prepared ultrashort echo time cones (3D IR-UTE-Cones) imaging of cortical bone in the hip. Magn Reson Imaging. 2017;In Press. doi:10.1016/j.mri.2017.07.012.

52. Burr DB, Turner CH, Naick P, et al. Does microdamage accumulation affect the mechanical properties of bone? J Biomech. 1998;31(4):337–345. doi:10.1016/S0021-9290(98)00016-5. [PubMed: 9672087]

53. Ma Y-J, Tadros A, Du J, Chang EY. Quantitative two-dimensional ultrashort echo time magnetization transfer (2D UTE-MT) imaging of cortical bone. Magnetic Resonance in Medicine. 2017.

54. Ramani A, Dalton C, Miller DH, Tofts PS, Barker GJ. Precise estimate of fundamental in-vivo MT parameters in human brain in clinically feasible times. Magn Reson Imaging. 2002;20(10):721–731. doi:10.1016/S0730-725X(02)00598-2. [PubMed: 12591568]

55. Biswas R, Bae WC, Diaz E, et al. Ultrashort echo time (UTE) imaging with bi-component analysis: Bound and free water evaluation of bovine cortical bone subject to sequential drying. Bone. 2012;50(3):749–755. doi:10.1016/j.bone.2011.11.029. [PubMed: 22178540]

56. Peris P Stress fractures. Best Pract Res Clin Rheumatol. 2003;17(6):1043–1061. doi:10.1016/S1521-6942(03)00114-1. [PubMed: 15123050]

57. Fredericson M, Bergman AG, Hoffman KL, Dillingham MS. Tibial stress reaction in runners correlation of clinical symptoms and scintigraphy with a new magnetic resonance imaging grading system. Am J Sports Med. 1995;23(4):472–481. http://ajs.sagepub.com/content/2¾/472.short. [PubMed: 7573660]

58. Pattin CA, Caler WE, Carter DR. Cyclic mechanical property degradation during fatigue loading of cortical bone. J Biomech. 1996;29(1):69–79. doi:10.1016/0021-9290(94)00156-1. [PubMed: 8839019]

59. Diab T, Vashishth D. Effects of damage morphology on cortical bone fragility. Bone. 2005;37(1):96–102. doi:10.1016/j.bone.2005.03.014. [PubMed: 15897021]

60. Landrigan MD, Li J, Turnbull TL, Burr DB, Niebur GL, Roeder RK. Contrast-enhanced micro-computed tomography of fatigue microdamage accumulation in human cortical bone. Bone. 2011;48(3):443–450. doi:10.1016/j.bone.2010.10.160. [PubMed: 20951850]
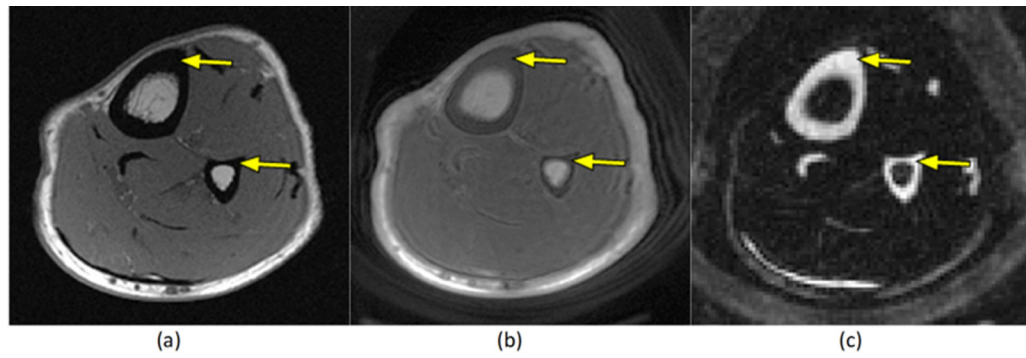
61. Turnbull TL, Gargac JA, Niebur GL, Roeder RK. Detection of fatigue microdamage in whole rat femora using contrast-enhanced micro-computed tomography. J Biomech. 2011;44(13):2395–2400. doi:10.1016/j.jbiomech.2011.06.032. [PubMed: 21764062]
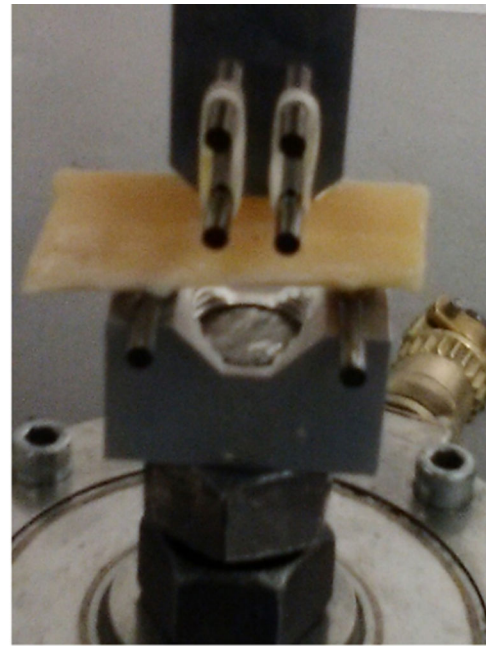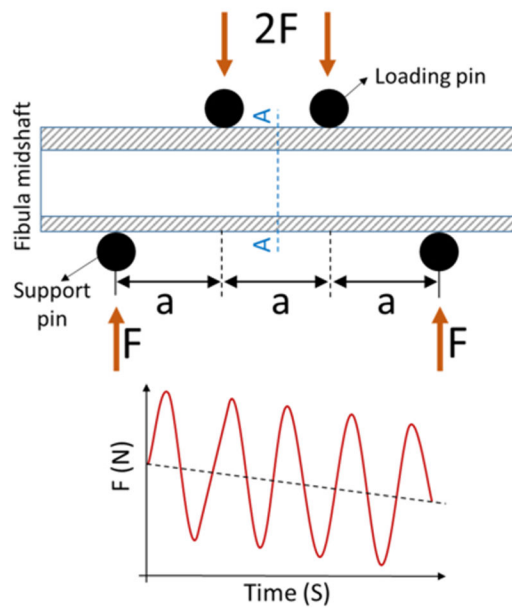
Figure 1:
Axial MR images of the leg of a healthy volunteer. (a) Clinical gradient echo sequence shows signal void in the tibial and fibular cortices (arrows). (b) UTE sequence with 32 μs echo time shows a high signal in the cortical bone (arrow). (c) IR-UTE sequence provides high contrast for the short T2* components of cortical bone (arrow), by selectively suppressing signal from fat and muscle.
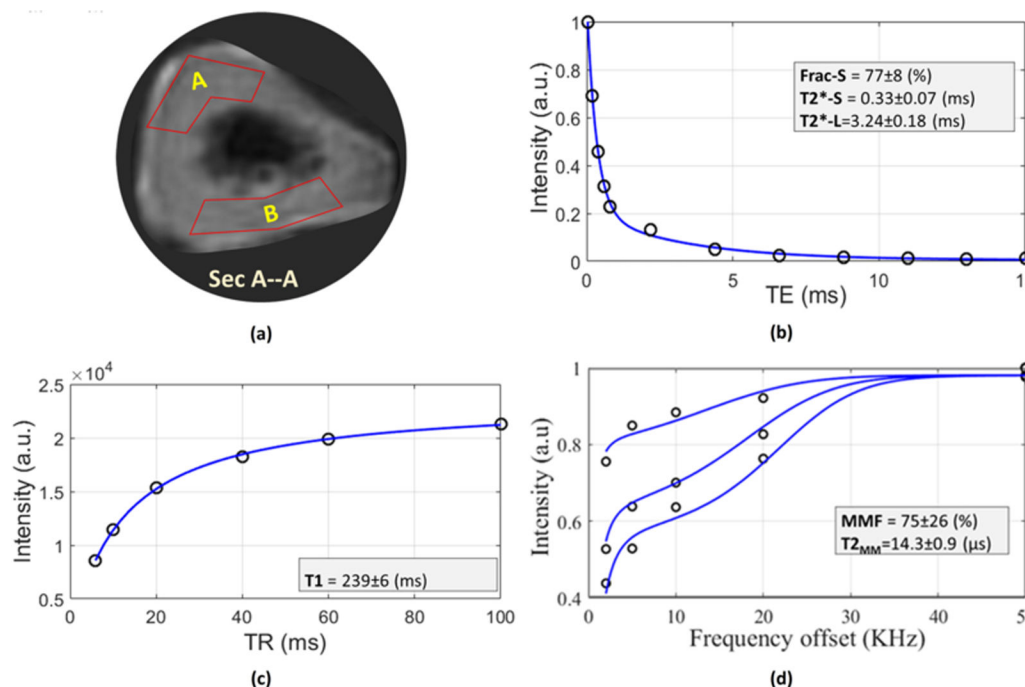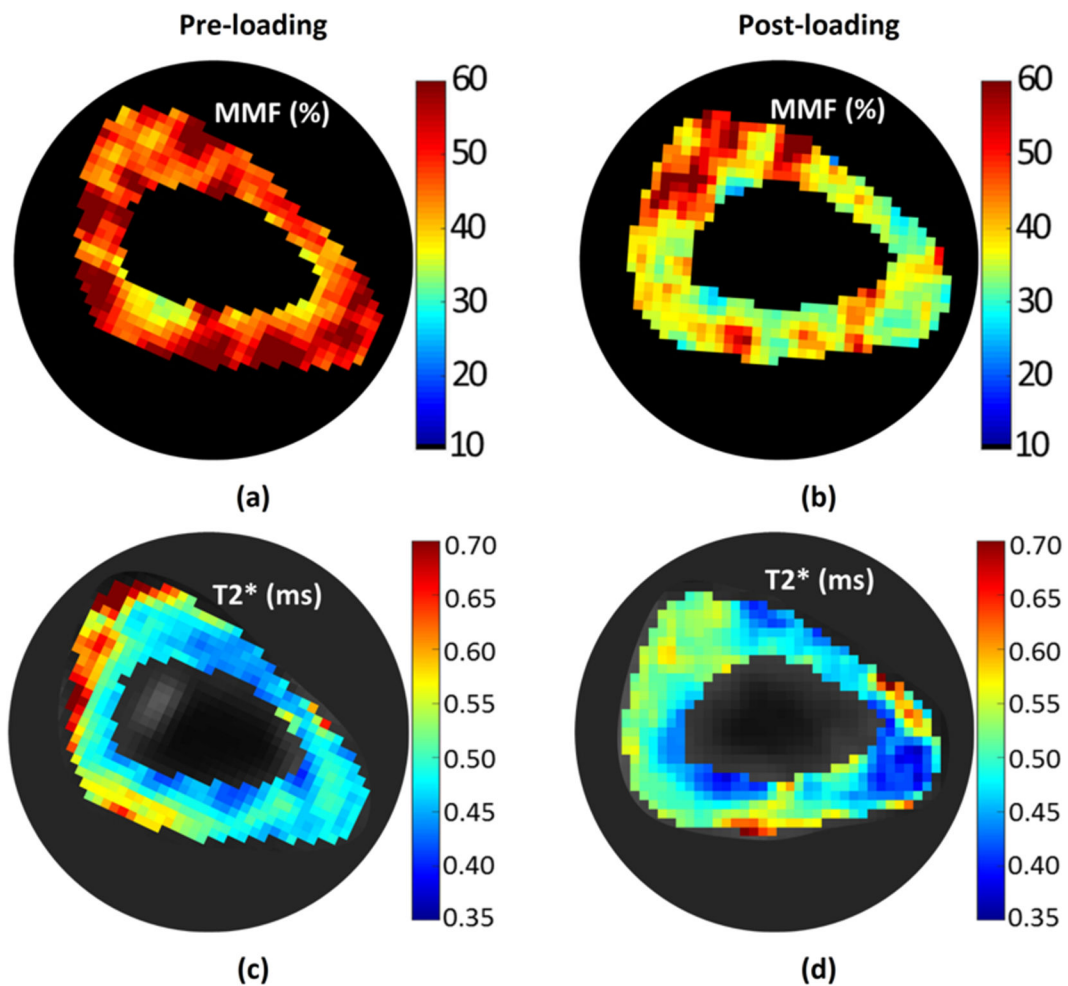
Figure 2:
Standard four-point bending setup to apply dynamic loads on fibular samples (hollow cylinder) at the midshaft. (a) Schematics of the four-point bending jigs at the longitudinal cross-section (a=8 mm, indenter diameter = 3 mm, fibular diameter=10 mm approx.). The experiments were displacement controlled (i.e., −5000±1500 μstrain) at 4 HZ and were stopped when 20% reduction of bone stiffness was achieved (2 hours approx.). A-A is a section between two loading pins, selected for UTE-MRI analyses. (b) Prepared fibular midshaft (4 cm approx.) under cyclic mechanical loading using the fabricated four-point bending jigs (Aluminum seats and Tungsten pins) mounted on an Instron 8511.20 machine.

Figure 3:
The MRI based analyses for a representative axial section in the middle of sample I (Section A-A shown in Figure 2a). The circle points and the solid lines in the sub-figures represent the average signal in the ROI and the fitted curves, respectively. (a) Two region of interests (ROIs A and B) were selected per each specimen. ROI-A was selected at compression side in 4-point bending test whereas ROI-B was at tension side. (b) Bi-component T2* signal decay analyses for differing TEs within a representative ROI-A (T2*-S, T2*-L and Frac-S refer to short T2*, long T2* and fraction of the short T2*, respectively). (c) T1 signal recovery analysis for differing TR from 5.7 up to 100 ms within selected ROI. (d) The two-pool MT modeling analyses using three pulse saturation powers (500, 750 and 1000 °) and five off-resonance frequencies (5, 10, 20, 50 KHz). MMF and $T2_{MM}$ refer to macromolecular fraction and macromolecular T2, respectively. Excellent fittings were obtained for T1, T2*, and MT curves for all of the ROIs.

Figure 4:
Pixel maps of (a,b) macromolecular fraction (MMF) and (c,d) single-component T2* for a representative sample (sample I), at pre- and post-loading stages. These two parameter have presented significant variation on average by ex vivo BSI (Table 2). The MMF and T2* decreases are obvious in whole section of sample I.

Table 1:

Average UTE-MRI results (Single- and bi-component T2*, T1, MT modeling, and MTR) for all 14 fibular specimens before and after loading. Compression side refers to the upper side the fibulas mounted in the 4-point bending tests however, the tension side refers to the lower side.

		Bi-com					MT Model		MTR-500 (%)			MTR-1000 (%)			MTR-1500 (%)		
		T2* (ms)	Frac-S (%)	T2*-S (ms)	T2*-L (ms)	T1 (ms)	MMF (%)	$T2_{MM}$ (μs)	2kHz	5kHz	10kHz	2kHz	5kHz	10kHz	2kHz	5kHz	10kHz
Average	Pre	0.57±0.23	75±13	0.34±0.04	4.1±1.1	231±35	61±13	15.1±1.3	26±5	14±3	11±2	46±9	32±7	24±5	51±9	39±9	30±7
	Post	0.49±0.16	78±9	0.31±0.05	7.3±13.6	236±34	53±11	14.8±0.9	22±5	12±3	9±3	42±9	30±6	23±5	49±9	37±6	29±5
Compression side	Pre	0.58±0.25	75±13	0.34±0.04	4.2±1.1	245±36	59±15	15.3±1.3	25±6	14±4	10±3	44±10	31±8	24±5	50±11	38±10	29±8
	Post	0.48±0.18	80±10	0.33±0.04	10.9±18.6	244±29	51±9	14.7±0.7	23±6	13±4	10±3	43±10	31±7	23±5	50±9	38±7	29±6
Tension side	Pre	0.57±0.21	75±13	0.33±0.03	4.1±1.1	217±27	64±11	14.8±1.3	27±4	15±2	11±2	47±7	33±5	24±4	53±7	40±7	31±6
	Post	0.50±0.14	77±8	0.29±0.06	3.7±1.0	228±36	55±12	14.9±1.1	22±5	12±3	9±2	42±8	30±5	23±4	48±8	37±6	29±5

Table 2:

Summarized variations (Mean±SD) in analyzed UTE-MRI-based biomarkers (Single-component T2*, Bi-component T2*, T1, UTE_MT modelling, and MTR) by cyclic loading experiment. Compression side refers to the upper side the fibulas mounted in the 4-point bending tests however, the tension side refers to the lower side. The positive and negative signs indicate the increases and decreases, respectively.

| | | Bi-com | | | T1 | MT Model | | MTR-500 | | | MTR-1000 | | | MTR-1500 | | |
	T2*	Frac-S	T2*-S	T2*-L	T1	MMF	T2$_{MM}$	2kHz	5kHz	10kHz	2kHz	5kHz	10kHz	2kHz	5kHz	10kHz
Average	−12±11 p=0.01	+7±15 p=0.38	−7±16 p=0.70	+68±269 p=0.20	+3±13 p=0.66	−12±20 p=0.02	−2±5 p=0.24	−12±20 p=0.05	−13±20 p=0.11	−10±22 p=0.22	−6±16 p=0.29	−3±17 p=0.31	−2±16 p=0.84	−3±15 p=0.55	−3±16 p=0.41	0±19 p=0.51
Compression side	−15±10 p=0.03	+7±11 p=0.40	−3±14 p=0.71	+141±365 p=0.12	0±13 p=0.70	−9±23 p=0.15	−4±5 p=0.19	−9±18 p=0.19	−8±20 p=0.37	−5±22 p=0.48	−2±13 p=0.77	1±16 p=0.84	−1±16 p=0.91	2±13 p=0.87	+1±14 p=0.98	+5±17 p=0.95
Tension side	−10±11 p=0.28	+6±19 p=1.00	−11±17 p=0.36	−5±33 p=0.57	+5±13 p=0.30	−14±15 p=0.08	1±5 p=0.76	−15±21 p=0.01	−18±18 p=0.02	−14±21 p=0.05	−10±17 p=0.07	−7±17 p=0.28	−4±17 p=0.68	−8±16 p=0.12	−7±17 p=0.22	−4±19 p=0.40

All the changes are in (%)

Table 3:

Average μCT-based porosities for 4 representative fibulae specimens in different ROIs at compression and tension side in the 4-point bending test.

Sample	Pre-loading				Post-loading			
	I	II	III	IV	I	II	III	IV
Average	1.9*	2.5	1.7	1.0	2.1	2.3	0.7	1.2
Compression side	2.2	0.9	1.1	0.7	3.0	1.13	0.9	1.3
Tension side	1.6	4.0	2.9	1.3	1.2	3.5	0.3	1.2

*
All values are in (%)